Scattering of plate waves by a cylindrical inhomogeneity

Chun H. Wang[a,b,*], Fu-Kuo Chang[b]

[a]*Air Vehicle Division, Defence Science and Technology Organisation, Melbourne, Australia*
[b]*Department of Aeronautics and Astronautics, Stanford University, Stanford, CA 94305, USA*

Abstract

To develop a quantitative in situ structural health-monitoring system, which measures the scattered wave field using piezoelectric sensors, that can determine the size and severity of structural anomaly in plate-like structures, it is important to characterize the interaction of plate waves with damages. This paper presents a theoretical and experimental investigation of the scattering behavior of extensional and flexural plate waves by a cylindrical inhomogeneity. Exact solutions are obtained by using the wave function expansion method, while the Born first approximation has been employed to derive explicit solutions that form the basis for efficient parametric inversion and eigenfunction back-propagation. To verify the analytical methods, experiments have been performed on a metallic plate, with a cylindrical mass being bonded to one side of the plate to simulate damage. Circular piezoelectric transducers were surface mounted on the plate to generate and measure stress waves. A good correlation has been observed between the analytical solutions and the experimental data. The present results reveal that the scattering pattern is strongly dependent on the ratio of wavelength to the size of the inhomogeneity, indicating the importance of selecting the appropriate diagnostic frequency as well as the optimal placement of sensors to achieve maximum sensor response.
© 2004 Published by Elsevier Ltd.

1. Introduction

For plate-like structures, guided waves (which is often called Lamb waves) have been the method of choice in both conventional non-destructive evaluation (using contact-based ultrasound

---

*Corresponding author. Aeronautical and Maritime Research Laboratory, Defence Science and Technology Organisation, 506 Lorimer Street, Fishermans Bend, Victoria 3207, Australia. Tel.: 61-3-9626-7125; fax: 61-3-9626-7089.

E-mail address: Chun.wang@dsto.defence.gov.au (C.H. Wang).

transducers or laser ultrasonics techniques) [1–5] and in situ structural health monitoring in which built-in active sensors are used to generate and measure guided waves [6–8]. Studies to date have shown that guided wave techniques can be applied to detect a variety of structural damages, including delamination in composite structures, corrosion damages, fatigue cracks, and debond in bonded joints. While most of the investigations have been qualitative in nature, attempts have been made to relate the measured wave fields to the size and severity of structural damages. In this regard, the scattering characteristics of structural damages are required to enable inverse solutions, such as parametric inversion or computerized tomography [9,10]. These results will also aid the optimal placement of sensors to achieve high signal-to-noise ratio.

Although the Rayleigh-Lamb solution for plate waves is exact, it is rather unwieldy for characterizing the interaction of plate waves with structural damages, due to the need to account for the effect of mode conversions among an infinite number of wave modes. It is known that even when the excitation frequency is below the cut-off frequency of the first-order modes (i.e. there is only one propagating wave), higher-order modes, which are near-field waves [11], participate in the mode conversion process at the interface between damages and the surrounding structure [12]. Recently Grahn [13] presented a numerical solution for a part-through hole by using a double series wave function expansion method. It was found that a high number of Lamb modes were needed to achieve convergence. For instance, at a moderately low frequency of one-third the cut-off frequency of the second flexural mode, a total of nine Lamb modes were required in the calculations. For higher frequencies, more terms would be needed in the expansions which would result in a slower convergence rate [13]. Therefore, a computationally more efficient method is required for inverse solutions.

As an alternative to the Lamb solution, higher-order plate theories, in particular the Kane–Mindlin extensional deformation theory [14] and the Mindlin plate bending theory [15], have been shown to provide a very accurate description of dispersive behavior of guided waves, both symmetric and anti-symmetric, up to the cut-off frequency of the second flexural wave mode [12,16]. At the low-frequency limit, the Mindlin plate theories reduce to the Poisson plate theory for extensional waves and the Kirchhoff plate theory for flexural waves, which will be collectively referred to as lower-order plate theories. In the case of scattering of extensional waves by circular inclusions, McKeon and Hinders [16] extended the lower-order plate theory solution of Pao [17] to the Kane–Mindlin plate extension theory. It is noted, however, the scattering amplitude for an open hole obtained by McKeon and Hinders differed significantly from those for a part-through hole reported by Grahn [13].

The analogous problem of scattering of flexural waves by circular inclusions was solved by Vemula and Norris for the Mindlin plate theory [18] as well as the lower-order Kirchhoff plate theory [19]. In their paper, Vemula and Norris [19] reported that at the low-frequency limit, scattering was mainly in the forward and backward directions, with very little side scattering. It is not clear, however, whether the scattering at higher frequencies, approaching the cut-off frequency of the second flexural mode, would follow the same trend. Some experimental results have been reported by Fromme and Sayie [20,21], which confirmed that the Mindlin plate theory is accurate in capturing the scattered wave field at the edge of an open hole. However, no experimental results could be located in the literature to verify the far-field scattering pattern by a circular hole or inclusions in general.

It is well recognized that the scattering of electromagnetic waves can be classified into three regimes [22], viz, the Rayleigh regime (wavelength much greater than target), the optical regime

(wavelength much less than target), and the resonance regime (wavelength comparable to target size). In the resonance regime, the scattering pattern or the radar cross-section is most complicated and difficult to predict, because the scattering pattern may vary significantly with the ratio of target size to wavelength. Since an in situ structural health monitoring system is intended to detect relatively small damage with size comparable to both the plate thickness and the wavelength of the guided waves that can be generated by built-in piezoelectric transducers, in situ structural health monitoring inevitably falls within the resonance regime. It is therefore essential to characterize the scattering pattern in this complex regime to help with the design of in situ health-monitoring systems and the interpretation of experimental measurements.

The purpose of this paper is to present solutions of the far-field scattering patterns of both extensional and flexural waves by a cylindrical inhomogeneity using the higher-order plate theories, with the results being compared to experimental data. In addition, a comparison will be made of the scattering patterns determined by the wave function expansion method, which can be viewed as exact solutions, and the Born approximation, with a view to determining the range of validity of the Born or Rytov approximations. Although the Born approximation is known to impose severe mathematical limitations to the range of objects that can be imaged, this approximation is fundamental to the image reconstruction process. For instance, both the plate-wave diffraction tomographic method developed by Rose and Wang [10,23,24] and the eigen function back-propagation method [25–27] rely on the Born approximation. Kak and Slaney [28] noted that in the case of pressure wave the *necessary* condition for the Born approximation to be valid is that the change in phase between the incident field and wave propagating through the target be less than π. This limitation implies that the target size needs to be less than the wavelength when the change in refractive index is equal to unity. It is yet unclear whether such a requirement also applies to guided waves.

This paper is structured as the following. Exact solutions for the scattering of extensional and flexural waves by a circular inhomogeneity are presented in Section 2. Approximate solutions based on the Born approximation are presented in Section 3. Comparisons between analytical solutions, the Born approximation, and experimental results are summarized in Sections 4 and 5, respectively.

2. Wave scattering by cylindrical inhomogeneity

Consider an infinite plate with a cylindrical inhomogeneity, representing either a delamination in a quasi-isotropic composite plate or a corrosion-induced thinning in a metallic plate. For simplicity, the properties of the inhomogeneity are assumed to be uniform through its thickness. Referring to Fig. 1, the problem being considered is an elastic plate of thickness h, containing a cylindrical inhomogeneity of a radius a and thickness h^* at the origin of a cylindrical coordinate system. The inhomogeneity, which can be viewed as representing either a delamination or a corrosion damage, as illustrated in Fig. 2. The inhomogeneity, shown in Fig. 2(c), has material properties (c_{ij}^*, ρ^*) that are different from those of the plate (c_{ij}, ρ). Here the parameters c_{ij} denote the stiffness matrix for a transversely isotropic material, and ρ the density.

Since the governing equations for the extensional and flexural deformations are uncoupled for inhomogeneities whose properties do not vary in the thickness direction, solutions of the
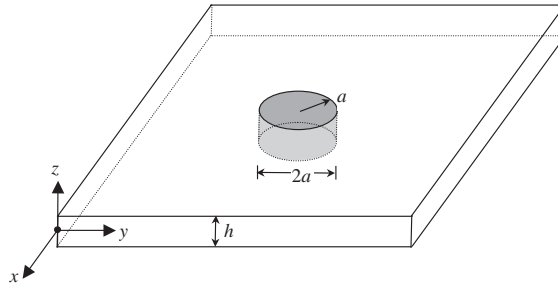
Fig. 1. Dimension and coordinate system for a plate containing a cylindrical inhomogeneity.
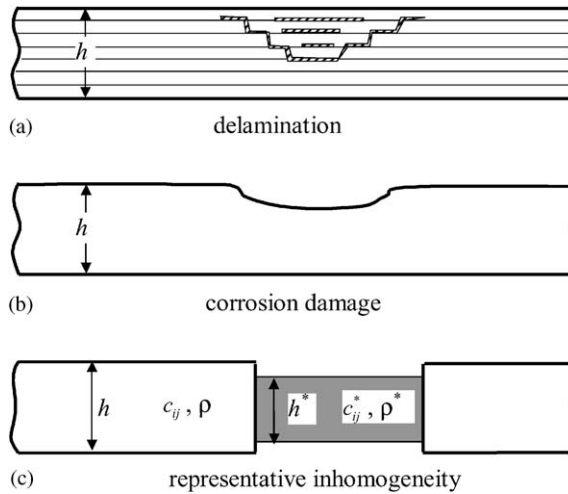

Fig. 2. Cross-section view of an inhomogeneity representing delamination and corrosion damages.

scattering patterns will be presented separately in the following two sub-sections. It is noted that the present method can be readily extended to analyze asymmetric damage, such as a part-through hole, by coupling the extensional and flexural waves through the continuity conditions at the interface between the inhomogeneity and the exterior plate.

2.1. Extensional wave

By assuming that the through-thickness strain is uniform through the plate thickness, Kane and Mindlin [14] developed a higher-order plate theory for the extensional waves in an isotropic plate. In the following, the Kane–Mindlin theory will be extended to the case of transversely isotropic material, following the method employed by Kotousov and Wang [29,30] for the static case.

In the Cartesian coordinate system shown in Fig. 1, the displacement fields take the following form:

$$u_x = v_x(x, y), \quad u_y = v_y(x, y), \quad u_z = v_z(x, y)\frac{2z}{h}. \tag{1}$$

Making use of the generalized Hooke's law for transversely isotropic medium (the plate is isotropic in the $x-y$ plane), the stress resultants (see Refs. [29, 30] for notations) can be expressed in terms of the displacement components, noting that h denotes the total thickness [29]

$$N_{xx} = h(c_{11}\varepsilon_{xx} + c_{12}\varepsilon_{yy} + 2c_{13}v_z/h), \tag{2a}$$

$$N_{yy} = h(c_{12}\varepsilon_{xx} + c_{11}\varepsilon_{yy} + 2c_{13}v_z/h), \tag{2b}$$

$$N_{zz} = h(\kappa c_{13}\varepsilon_{xx} + \kappa c_{13}\varepsilon_{yy} + 2\kappa^2 c_{33}v_z/h), \tag{2c}$$

$$N_{xy} = h\frac{c_{11} - c_{12}}{2}\varepsilon_{xy}, \tag{2d}$$

$$R_x = c_{44}\frac{h^2}{6}\frac{\partial v_z}{\partial x}, \tag{2e}$$

$$R_y = c_{44}\frac{h^2}{6}\frac{\partial v_z}{\partial y}, \tag{2f}$$

where $\kappa = \pi/\sqrt{12}$ and the constants $(c_{11}, c_{12}, c_{13}, c_{33}, c_{44})$ are the elastic constants. Inserting the above expressions into the equations of motion yields the following equations for the case of zero body forces:

$$c_{11}\frac{\partial^2 v_x}{\partial x^2} + c_{12}\frac{\partial^2 v_y}{\partial x\partial y} + \frac{2\kappa c_{13}}{h}\frac{\partial v_z}{\partial x} + \frac{c_{11} - c_{12}}{2}\left(\frac{\partial^2 v_x}{\partial y^2} + \frac{\partial^2 v_y}{\partial x\partial y}\right) = \rho\frac{\partial^2 v_x}{\partial t^2}, \tag{3a}$$

$$\frac{c_{11} - c_{12}}{2}\left(\frac{\partial^2 v_x}{\partial x\partial y} + \frac{\partial^2 v_y}{\partial x^2}\right) + c_{12}\frac{\partial^2 v_x}{\partial x\partial y} + c_{11}\frac{\partial^2 v_y}{\partial y^2} + \frac{2\kappa c_{13}}{h}\frac{\partial v_z}{\partial y} = \rho\frac{\partial^2 v_y}{\partial t^2}, \tag{3b}$$

$$\frac{h^2}{6}c_{44}\nabla^2 v_z - h\kappa c_{13}\left(\frac{\partial v_x}{\partial x} + \frac{\partial v_y}{\partial y}\right) - 2\kappa^2 c_{33}v_z = \tfrac{1}{6}\rho h^2\frac{\partial^2 v_z}{\partial t^2} \tag{3c}$$

The cut-off frequency ω_e of the second extensional wave can be determined from Eq. (3c) by letting $v_z = Ce^{i\omega_e t}$, $v_x = v_y = 0$, which represents a purely thickness mode

$$\omega_e = \sqrt{\frac{12\kappa^2}{h^2}\frac{c_{33}}{\rho}}. \tag{4}$$

Since the transverse stiffness of most quasi-isotropic composite laminates is much lower than the in-plane stiffness, the above solution suggests that the cut-off frequency of transversely isotropic material could be considerably lower than that of the equivalent isotropic material. Therefore, it is important to account for the influence of this lower cut-off frequency on the dispersion behavior of the extensional waves.

To determine the dispersion relationship for a transversely isotropic material, let us express the in-plane displacement components in terms of two potentials, φ and ψ,

$$v_x = \frac{\partial \varphi}{\partial x} + \frac{\partial \psi}{\partial y}, \tag{5a}$$

$$v_y = \frac{\partial \varphi}{\partial y} - \frac{\partial \psi}{\partial x}. \tag{5b}$$

Then, Eqs. (3a–b) can be satisfied after introducing a time factor $e^{-i\omega t}$ that will be omitted in the following, if

$$\nabla^2 \psi + k_3^2 \psi = 0, \tag{6a}$$

$$c_{11}\nabla^2\varphi + \rho\omega^2\varphi + \frac{2\kappa c_{13}}{h}v_z = 0, \tag{6b}$$

$$c_{44}\nabla^2 v_z + \rho(\omega^2 - \omega_e^2)v_z - \frac{6}{h}\kappa c_{13}\nabla^2\varphi = 0 \tag{6c}$$

with

$$k_3^2 = \frac{2\rho\omega^2}{c_{11} - c_{12}}. \tag{6d}$$

It can be seen that the present solution does recover the Kane–Mindlin solution in the special case of isotropic plate [14] by setting $c_{11} = c_{33} = \lambda + 2\mu$, $c_{12} = c_{13} = \lambda$, and $c_{44} = \mu$.

Eliminating v_z between Eqs. (6b) and (6c), the equation governing φ is found to be

$$\nabla^4\varphi + 2B\nabla^2\varphi + C\varphi = 0 \tag{7a}$$

with

$$B = \frac{\rho\omega^2}{2c_{11}} + \frac{\rho(\omega^2 - \omega_e^2)}{2c_{44}} + \frac{6\kappa^2 c_{13}^2}{h^2 c_{11} c_{44}}, \tag{7b}$$

$$C = \frac{(\omega^2 - \omega_e^2)\rho^2\omega^2}{c_{11}c_{44}}. \tag{7c}$$

Inserting $\varphi = e^{ikx}$ into Eq. (7a), the following wave numbers k are obtained:

$$k_1^2 = B + \sqrt{B^2 - C}, \tag{8a}$$

$$k_2^2 = B - \sqrt{B^2 - C}. \tag{8b}$$

Since Poisson's ratio has only a very minor influence on the values of the wave numbers, the major deviation of the dispersion relationship from that of isotropic material is due to the lower modulus in the thickness direction. An example is shown in Fig. 3 to illustrate the difference in the dispersion curves between a transversely isotropic material and the equivalent isotropic material whose properties are identical to the in-plane properties of the transversely isotropic material. It can be seen that the approximately non-dispersive region (where group velocity is nearly
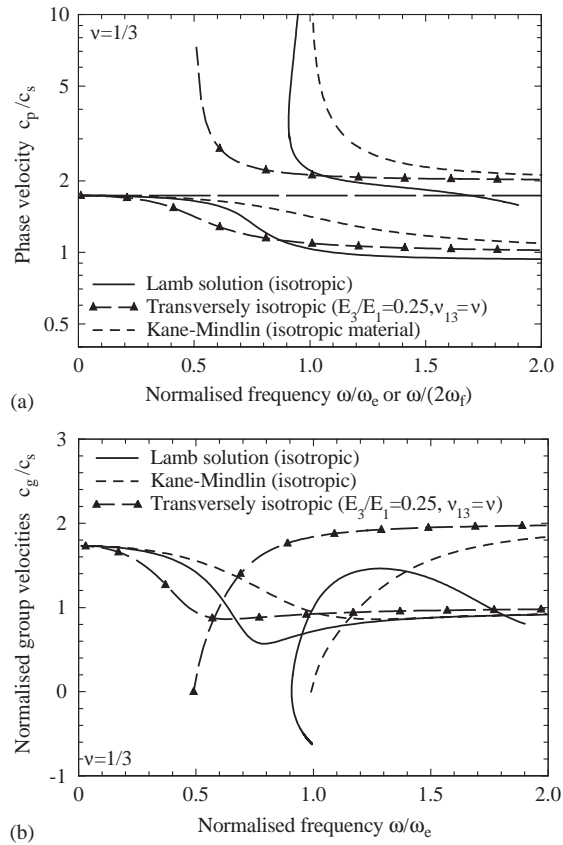
Fig. 3. Dispersion curves of extensional waves in transversely isotropic material. (a) phase velocity and (b) group velocity. The frequency is normalized by the cut-off frequency of the equivalent isotropic material.

independent of frequency) has shrunk significantly as a result of reduction in the cut-off frequency of the second mode. It is also interesting to note from Eq. (7) that the dispersion curve of the transversely isotropic material would trace over that of the equivalent isotropic material when the frequency is normalized by the cut-off frequency of the transversely isotropic material.

Since k_1 is never equal to k_2, it is advantageous to decompose the displacement potential φ into two potentials, φ_1 and φ_2, where $\varphi = \varphi_1 + \varphi_2$. Here $\nabla^2 \varphi_i + k_i^2 \varphi_i = 0$, $i = 1, 2$. Now the plate displacement components can be expressed in terms of three potentials, noting Eq. (6b) for v_z,

$$v_x = \left(\frac{\partial \varphi_1}{\partial x} + \frac{\partial \varphi_2}{\partial x} + \frac{\partial \psi}{\partial y} \right) e^{-i\omega t}, \tag{9a}$$

$$v_y = \left(\frac{\partial \varphi_1}{\partial y} + \frac{\partial \varphi_2}{\partial y} - \frac{\partial \psi}{\partial x} \right) e^{-i\omega t}, \tag{9b}$$

$$v_z = \left(\sigma_1 \varphi_1 + \sigma_2 \varphi_2 \right) e^{-i\omega t}, \tag{9c}$$

where

$$\sigma_i = \frac{hc_{11}}{2\kappa c_{13}}\left(k_i^2 - \frac{\rho\omega^2}{c_{11}}\right), \quad i = 1, 2. \tag{9d}$$

Consider an incident plane wave traveling in the positive x direction, $v_x = e^{ik_1 x}$, suppressing $e^{-i\omega t}$ in the sequel. The displacement potentials for the incident wave can be written as

$$\varphi_1^{(i)} = -ie^{ik_1 x}/k_1 = \sum_{n=0}^{\infty} \epsilon_n i^{n-1} J_n(k_1 r)\cos(n\theta)/k_1, \quad \varphi_2^{(i)} = H^{(i)} = 0, \tag{10}$$

where the superscript i denotes parameters pertaining to the incident wave, and

$$\epsilon_n = \begin{cases} 1, & n = 0, \\ 2, & n \geqslant 1. \end{cases} \tag{11}$$

Following the standard wave function expansion method [16,18,31], the general solutions of the scattered wave and the wave inside a circular scatterer at the origin of a cylindrical coordinate system can be expressed as in terms of Hankel and Bessel functions.

$$\varphi_1^{(s)} = \sum_{n=0}^{\infty} A_n H_n(k_1 r)\cos n\theta, \quad \varphi_2^{(s)} = \sum_{n=0}^{\infty} B_n H_n(k_2 r)\cos n\theta, \quad \psi^{(s)} = \sum_{n=0}^{\infty} C_n H_n(k_3 r)\sin n\theta, \tag{12a}$$

$$\varphi_1^{(t)} = \sum_{n=0}^{\infty} D_n J_n(k_1 r)\cos n\theta, \quad \varphi_2^{(t)} = \sum_{n=0}^{\infty} E_n J_n(k_2 r)\cos n\theta, \quad \psi^{(t)} = \sum_{n=0}^{\infty} F_n J_n(k_3 r)\sin n\theta, \tag{12b}$$

where the superscript t denotes parameters pertaining to the wave field transmitted into the scatterer. The six sets of unknown coefficients $A_n, B_n, C_n, D_n, E_n, F_n$ are to be determined from the continuity conditions at $r = a$,

$$v_r^{(i)} + v_r^{(s)} = v_r^{(t)}, \quad v_\theta^{(i)} + v_\theta^{(s)} = v_\theta^{(t)}, \quad (v_z^{(i)} + v_z^{(s)})\frac{h^*}{h} = v_z^{(t)}, \tag{13a}$$

$$N_{rr}^{(i)} + N_{rr}^{(s)} = N_{rr}^{(t)}, \quad N_{r\theta}^{(i)} + N_{r\theta}^{(s)} = N_{r\theta}^{(t)}, \quad R_{rz}^{(i)} + R_{rz}^{(s)} = R_{rz}^{(t)}. \tag{13b}$$

The linear set of equations (13a) and (13b) can be readily solved numerically or by using symbolic manipulation software Mathematica [32]. For frequencies below the cut-off frequency of second extensional wave, both k_2 and k_3 are purely imaginary, so there is only one outgoing wave radiating from the scatterer. Therefore, the far-field ($k_1 r \to \infty$) scattered wave is given by

$$u_r^{(s)}(r, \theta) = ik_1 \sum_{n=0}^{\infty} A_n \sqrt{\frac{2}{\pi k_1 r}} e^{i[k_1 r - (1+2n)\pi/4]}\cos n\theta \equiv \sqrt{\frac{2}{\pi k_1 r}} e^{i[k_1 r - \pi/4]}S_1(\theta), \tag{14}$$

where the asymptotic expansion $\lim_{x\to\infty} H_n(x) = \sqrt{2/\pi x}\, e^{i[x-(1+2n)\pi/4]}$ has been used. The function $S_1(\theta)$ denotes the far-field scattering amplitude for an incident extensional wave of unity strength

$$S_1(\theta) = ik_1 \sum_{n=0}^{\infty} A_n e^{-in\pi/2}\cos n\theta. \tag{15}$$

A parametric analysis reveals that the coefficients A_n depend on a large number of variables including k_1a, k_2a, k_3a, k_1^*a, k_2^*a, k_3^*a, h^*/h, and moduli c_{ij} and c_{ij}^*. Since the transverse properties and Poisson's ratios only weakly influence the wave numbers, the scattering pattern is dominated by four non-dimensional parameters, k_1a, h^*/h, ω/ω_{ce}, and $\omega_{ce}^*/\omega_{ce}$, where ω_{ce} denotes the cut-off frequency of the second extensional mode. Numerical results and comparisons with experimental data will be discussed in Section 4.

2.2. Flexural wave

The following solution follows closely the method employed by Vemula and Norris [18], but using a slightly different formulation to facilitate parametric analysis as well as the sake of consistency with the solution method for extensional wave. Adopting the method of Rose and Wang [10], the governing equations for flexural waves depend on four properties, bending stiffness D, rotary inertia ρI, deflection inertia ρh, and shear stiffness μh. The wave field is given in terms of the deflection w and two potentials ϕ and ψ, with the angle of rotations being given by

$$\Omega_r = \frac{\partial \phi}{\partial r} + \frac{1}{r}\frac{\partial \psi}{\partial \theta}, \tag{16a}$$

$$\Omega_\theta = \frac{1}{r}\frac{\partial \phi}{\partial \theta} - \frac{\partial \psi}{\partial r}. \tag{16b}$$

The governing equations for the two potentials ϕ and ψ were given by Rose and Wang [10], from which the wave numbers can be determined as following

$$k_{1,2}^2 = \omega^2(B \pm \sqrt{B^2 - C}), \tag{17a}$$

$$k_3^2 = 2\frac{\rho I \omega^2 - \mu h}{D(1-v)}, \tag{17b}$$

with

$$B = \frac{1}{2}\left(\frac{\rho I}{D} + \frac{\rho h}{\mu h}\right), \tag{18a}$$

$$C = \frac{\rho I}{D}\frac{\rho h}{\mu h} - \frac{\rho h}{D}\frac{1}{\omega^2}. \tag{18b}$$

Consider an incident plane wave traveling in the positive x direction, $w = e^{ik_1x}$, suppressing $e^{-i\omega t}$ in the sequel. The displacement potentials for the incident wave can be written as

$$w^{(i)} = e^{ik_1x} = \sum_{n=0}^{\infty} \in_n i^n J_n(k_1 r)\cos(n\theta), \quad \phi^{(i)} = \gamma_1 w, \quad \psi^{(i)} = 0. \tag{19}$$

The general solutions of the scattered wave and the wave inside a circular scatterer can be expressed as

$$w^{(s)} = \sum_{n=0}^{\infty} A_n H_n(k_1 r) \cos n\theta + B_n H_n(k_2 r) \cos n\theta, \tag{20a}$$

$$\varphi^{(s)} = \sum_{n=0}^{\infty} \gamma_1 A_n H_n(k_1 r) \cos n\theta + \gamma_2 B_n H_n(k_2 r) \cos n\theta, \tag{20b}$$

$$\psi^{(s)} = \sum_{n=0}^{\infty} C_n H_n(k_3 r) \cos n\theta, \tag{20c}$$

$$w^{(t)} = \sum_{n=0}^{\infty} D_n J_n(k_1 r) \cos n\theta + E_n J_n(k_2 r) \cos n\theta, \tag{20d}$$

$$\varphi^{(t)} = \sum_{n=0}^{\infty} \gamma_1 D_n J_n(k_1 r) \cos n\theta + \gamma_2 E_n J_n(k_2 r) \cos n\theta, \tag{20e}$$

$$\psi^{(t)} = \sum_{n=0}^{\infty} F_n J_n(k_3 r) \cos n\theta, \tag{20f}$$

where

$$\gamma_1 = 1 - \frac{\rho}{\kappa^2 \mu} \frac{\omega^2}{k_1^2}, \quad \gamma_2 = 1 - \frac{\rho}{\kappa^2 \mu} \frac{\omega^2}{k_2^2}. \tag{21}$$

The coefficients $A_n, B_n, C_n, D_n, E_n, F_n$ are to be determined from the following continuity and equilibrium conditions at the inhomogeneity-plate interface $r = a$:

$$w^{(i)} + w^{(s)} = w^{(t)}, \quad \Omega_r^{(i)} + \Omega_r^{(s)} = \Omega_r^{(t)}, \quad \Omega_\theta^{(i)} + \Omega_\theta^{(s)} = \Omega_\theta^{(t)}, \tag{22a}$$

$$M_{rr}^{(i)} + M_{rr}^{(s)} = M_{rr}^{(t)}, \quad M_{r\theta}^{(i)} + M_{r\theta}^{(s)} = M_{r\theta}^{(t)}, \quad Q_r^{(i)} + Q_r^{(s)} = Q_r^{(t)}. \tag{22b}$$

The resulting equations can be solved by either matrix inversion method or using symbolic manipulation software Mathematica [32].

With both k_2 and k_3 being purely imaginary below the cut-off frequency of second flexural wave, there is only one propagating wave radiating from the scatterer that contributes to the far-field scattering field. In this case, the far-field ($k_1 r \to \infty$) scattered wave is given by

$$w^{(s)}(r, \theta) = \sum_{n=0}^{\infty} A_n \sqrt{\frac{2}{\pi k_1 r}} e^{i[k_1 r - (1+2n)\pi/4]} \cos n\theta \equiv \sqrt{\frac{2}{\pi k_1 r}} e^{i[k_1 r - \pi/4]} S_2(\theta), \tag{23}$$

where $S_2(\theta)$ denotes the far-field scattering amplitude for an incident flexural wave of unit strength,

$$S_2(\theta) = \sum_{n=0}^{\infty} A_n e^{-in\pi/2} \cos n\theta. \tag{24}$$

It is noted that the present definition of the scattering amplitude is different from that employed by Vemula and Norris [18]. As will be shown later, this new definition, which is consistent with the scattering amplitude for the extensional wave, will ensure that the scattering amplitude will not diverge in the limit of rigid inclusion as encountered by Vemula and Norris [18].

Similar to the case of extensional wave, a parametric analysis suggests that the scattering amplitude is dependent on six non-dimensional variables $k_1 a$, a/h, $(\rho I)^*/\rho I$, D^*/D, $(\mu h)^*/\mu h$, and ω/ω_c, where ω_c denotes the cut-off frequency of the second flexural wave

$$\omega_c = \kappa \sqrt{\frac{\mu h}{\rho I}}. \tag{25}$$

For specific damage modes, such as corrosion damage or delamination damage, fewer non-dimensional parameters need to be considered. This will be further discussed in the next section.

3. Solution by the Born approximation

It is apparent that the exact solutions presented in the preceding sections are applicable to only simple geometries, such as cylindrical or elliptical scatterers. Furthermore, the complex dependence of the scattered wave fields on the properties and dimensions of the inhomogeneity renders it impractical to develop an efficient inverse solution method that can account for the effect of diffraction. Because of this difficulty, most of the inverse solutions, such as the computerized tomography [10, 23, 24, 28] and the eigenfunction backpropagation method [25–26, 33] inevitably rely on the use of the Born or Rytov approximations. In the following, the validity of the Born approximation to guided waves will be assessed by comparing the Born solution with the exact solution presented in the preceding sections for the special case of a cylindrical scatterer.

For the inhomogeneity, it is convenient to represent its properties in terms of those corresponding to the exterior plate in the following form

$$D^* = (1 + \delta_1)D, \tag{26a}$$

$$(\mu h)^* = (1 + \delta_2)\mu h, \tag{26b}$$

$$(\rho I)^* = (1 + \delta_3)\rho I, \tag{26c}$$

$$(\rho h)^* = (1 + \delta_4)\rho h. \tag{26d}$$

The variations δ_n ($n = 1,2,3,4$) are non-zero inside the inhomogeneity but vanish outside it. It is noted that these plate-theory parameters are not material properties: they depend also on the thickness h. Consider, for example, the bending stiffness $D = E'I$, where E' denotes the plane-strain Young's modulus and I the moment of inertia ($I = h^3/12$). A variation in D could result

from a variation in the Young's modulus E, due for instance to fiber fracture, or it could result from a variation in thickness h due to corrosion thinning, or it could be the result of variation in I due to delamination [12], without a change in the overall plate thickness h. So in general all four variations could be non-zero, and their precise values for a given damage mechanism need to be measured experimentally.

By applying the Born approximation to the Mindlin plate theory [23,24], the scattered wave of an incident plane wave from the left of an inhomogeneity, recalling Eq. (19), can be expressed as, referring to Fig. 4 for the coordinate system,

$$\hat{w}^B(x,\omega) = \int\int \left\{ \delta_1 D\Gamma^{(i)}_{\beta\alpha} g_{3\alpha,\beta} - \delta_2\mu h(w^{(i)}_{,\alpha} - \Omega^{(i)}_\alpha)(g_{3\alpha} + g_{33,\alpha}) \right.$$
$$\left. - \delta_3\rho I\omega^2\Omega^{(i)}_\alpha g_{3\alpha} + \delta_4\rho h\omega^2 w^{(i)} g_{33} \right\} \, d\xi \, d\zeta, \tag{27}$$

where the comma indicates differentiation with respect to coordinate ξ ($\alpha = 1$) or ζ ($\alpha = 2$). The above integration is performed over the scatterer. The relevant Green's functions g_{31}, g_{32}, and g_{33} are given by

$$g_{31} = \frac{i}{4D(k_1^2 - k_2^2)} \frac{\partial H_0(k_1 r')}{\partial x}, \tag{28a}$$

$$g_{32} = \frac{i}{4D(k_1^2 - k_2^2)} \frac{\partial H_0(k_1 r')}{\partial y}, \tag{28b}$$

$$g_{33} = \frac{i}{4D(k_1^2 - k_2^2)} \frac{H_0(k_1 r')}{\gamma_1}, \tag{28c}$$

with $r' = \sqrt{(x - \xi)^2 + (y - \zeta)^2}$. By taking the far-field asymptotic expression of the Hankel function, it can be shown that the Born solution corresponding to an incident plane wave given by Eq. (19) reduces to

$$\hat{w}^{(B)} = \left[\delta_1 p_1(\theta) + \delta_2 p_2(\theta) + \delta_3 p_3(\theta) + \delta_4 p_4(\theta) \right] t(\theta) \sqrt{\frac{2}{\pi k_1 r}} \, e^{i(k_1 r - \pi/4)}, \tag{29}$$
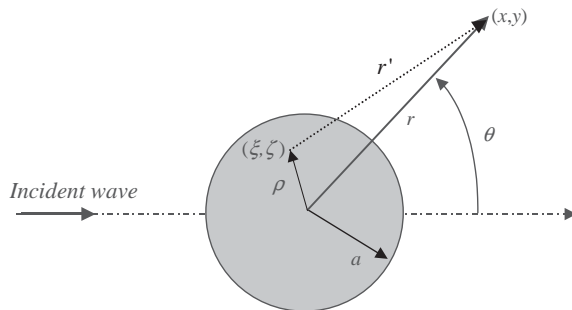

Fig. 4. An incident wave impinging on a cylindrical scattered.

where

$$p_1(\theta) = -\mathrm{i}\frac{\gamma_1 k_1^2}{4(k_1^2 - k_2^2)}\left[\cos^2\theta + v\sin^2\theta\right], \tag{30a}$$

$$p_2(\theta) = -\mathrm{i}\frac{\mu h(1 - \gamma_1)^2}{4\gamma_1 D(k_1^2 - k_2^2)}\cos\theta, \tag{30b}$$

$$p_3(\theta) = \mathrm{i}\frac{\gamma_1 \rho I\omega^2}{4D(k_1^2 - k_2^2)}\cos\theta, \tag{30c}$$

$$p_4(\theta) = \mathrm{i}\frac{\rho h\omega^2}{4\gamma_1 Dk_1^2(k_1^2 - k_2^2)}, \tag{30d}$$

$$t(\theta) = k_1^2 \int\int \mathrm{e}^{\mathrm{i}k_1\xi}\mathrm{e}^{\mathrm{i}k_1(r'-r)}\,\mathrm{d}\xi\,\,\mathrm{d}\zeta. \tag{30e}$$

For a cylindrical scatterer of radius a, explicit expression can be obtained for the function $t(\theta)$, noting the far-field expansion $r' - r = -\xi\cos\theta - \zeta\sin\theta$, referring to Fig. 4,

$$t(\theta) = k_1^2 \int_0^a \rho\,\mathrm{d}\rho \int_0^{2\pi} \mathrm{e}^{\mathrm{i}k_1\rho[(1-\cos\theta)\cos\phi - \sin\phi]}\mathrm{d}\phi = 2\pi k_1 a\frac{J_1(\sqrt{2 - 2\cos\theta}k_1 a)}{\sqrt{2 - 2\cos\theta}}. \tag{31}$$

Comparing to the wave function expansion method, it is clear that the Born approximation yields a closed-form solution of the scattering pattern. Furthermore, this scattering pattern depends only on two non-dimensional parameters, ω/ω_c and $k_1 a$. Since the function $t(\theta)$ describes how the shape of the scattering pattern evolves with $k_1 a$, it is useful to consider this shape function in more detail, which is shown in Fig. 5. It can be seen that the scattering pattern becomes increasingly skewed towards forward scattering at higher value of $k_1 a$. In particular, the forward- and the back-scattering component of the function $t(\theta)$ are given by

$$t(0) = \pi(k_1 a)^2, \tag{32a}$$

$$t(\pi) = \pi k_1 a J_1(2k_1 a). \tag{32b}$$

Therefore, it is clear that the forward-scattering component increases rapidly with $k_1 a$, while the backward-scattering component fluctuates as $k_1 a$ increases.

4. Numerical results of scattering patterns

The analysis presented in the preceding section suggests that it is possible to obtain quantitative information about the size and severity of structural damages through exploiting the variations in scattering patterns by varying the frequency thus the wavelength of the diagnostic wave. In this context, previous studies on beam structures [12] found that there is a strong stop-pass behavior, viz, the amount of reflection and transmission depends strongly on the ratio of damage length to wavelength. In the following the analytical methods presented in the preceding section will be
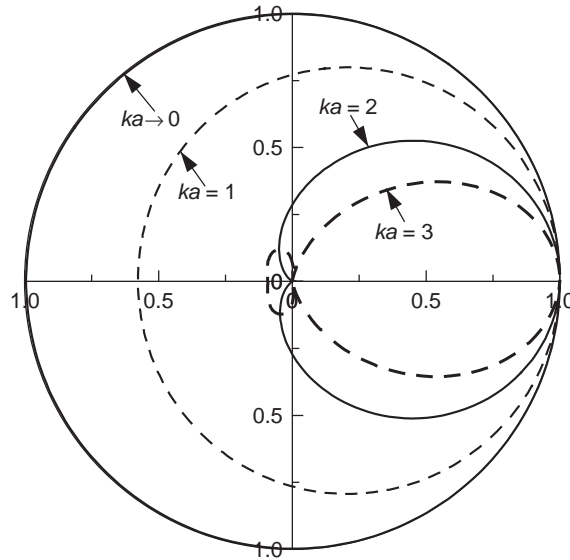
Fig. 5. Polar plot of normalized function $t(\theta)/t(\theta=0)$.

employed to investigate the scattering patterns of incident extensional and flexural waves by a circular damage. Two important cases of laminar damage representing corrosion damage in metallic structures and delamination of composite structures will be considered.

4.1. Extensional wave

Consider the case of corrosion damage that causes a 20% reduction in cross-sectional thickness. The following simulations are performed for an aluminium alloy with a Poisson's ratio of 0.3. The numerical results will be presented in terms of non-dimensional parameters ($k_1 a$ and ω/ω_e), so they are also applicable to composite structures experiencing degradation in in-plane stiffness as a result of impact damage, for example. Shown in Fig. 6 are the scattering patterns applicable to the low-frequency limit $\omega/\omega_e \leqslant 0.1$. It is seen that the scattering patterns vary significantly as the ratio of damage size to wavelength increases. The absolute magnitude of the scattered wave increases with $k_1 a$, but the strength of the forward-scattering (shadow) remains a small fraction of the back-scattering (echo). However, at the high-frequency limit ($\omega = \omega_e$), as shown in Fig. 7, the scattering pattern changes from echo-dominated to shadow dominated with the increase of $k_1 a$. One important implication of these results is that it would be possible determine the size of the damage by measuring the changes in scattering patterns with the diagnostic frequency.

Of particular interests are the magnitudes of the back- and forward-scattering amplitude, which are shown in Fig. 8 for three different diagnostic frequencies. At the low-frequency limit, the back-scattering magnitude oscillates more rapidly with $k_1 a$ than the forward-scattering magnitude. It should be noted that these results are for the case of single frequency. When the diagnostic signal is narrow-banded, such as tone-burst modulated by Hanning window [12], the response would exhibit a weaker fluctuation due to the frequency averaging effect.
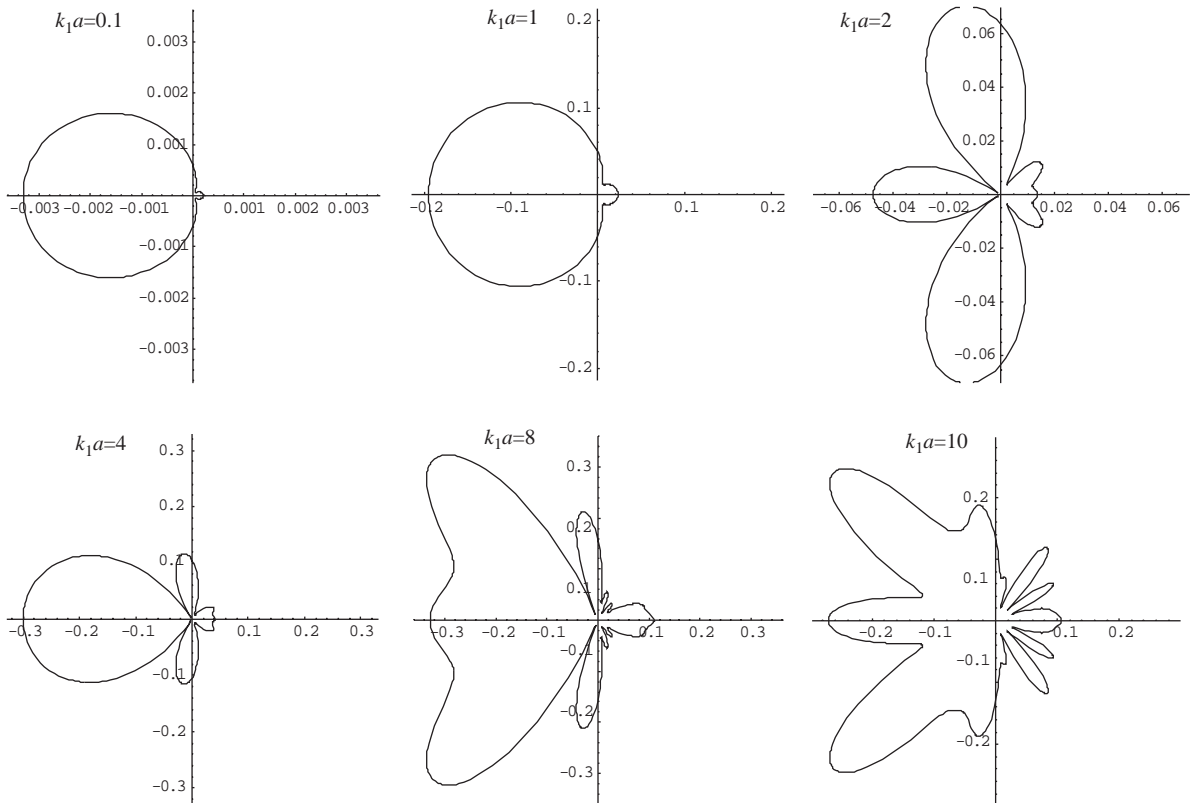
Fig. 6. Scattering pattern ($|S_1(\theta, k_1 a)|$) of extension waves by a corrosion damage (20% reduction in thickness) at low frequency ($\omega/\omega_e = 0.1$).

4.2. Flexural wave

As discussed in the preceding section, the scattering of flexural wave is dominated by changes in the bending stiffness. In the following the scattering patterns will be determined for the corrosion damage case considered in the previous section and a delamination damage, which is simulated by a reduced flexural stiffness ($D^* = D/4$), representing a single delamination damage [12]. The scattering patterns pertaining to the simulated corrosion damage are shown in Fig. 9, together with predictions by the Born approximation. It can be seen in the limit of very small damage (2% reduction in thickness), the Born approximation solution agrees with the exact solution. However, at 20% reduction in thickness, the Born approximation solution under-predicts the magnitude of the scattering amplitude. Nevertheless, the overall shape of the scattering pattern correlates reasonably well with the exact solution. Similar to the case of extensional waves, the scattering of flexural wave becomes more skewed towards forward scattering as ka increases, casting an increasingly larger shadow with negligible echo.

The scattering patterns for the case of delamination damage are shown in Fig. 10. Again, the same shadowing behavior is observed at high ka values. Since the flexural stiffness of the damaged
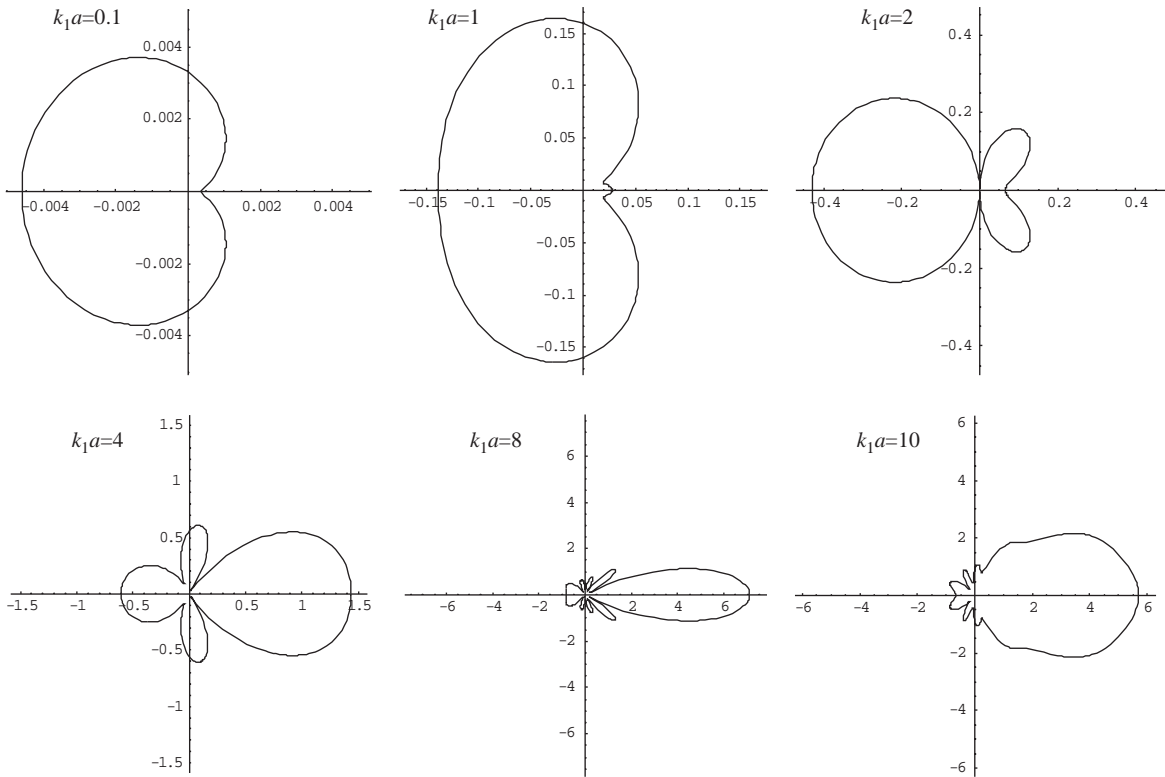
Fig. 7. Scattering pattern ($|S_1(\theta, k_1 a)|$) of extensional waves by a corrosion damage (20% reduction in thickness) at high frequency ($\omega/\omega_e = 1.0$).
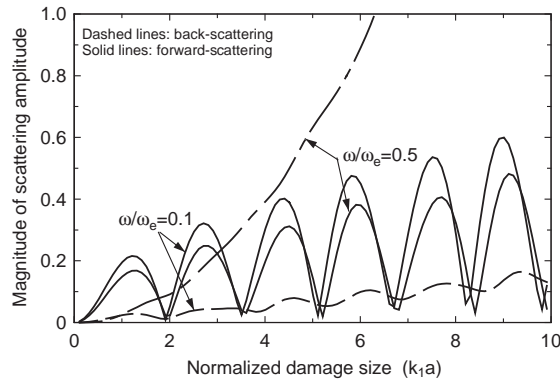

Fig. 8. Magnitudes of back- and forward-scattering amplitudes of extensional wave at two different frequencies.

region is only 25% of the base plate, this case is strictly speaking beyond the scope of Born approximation. Nevertheless, the Born approximation did yield a good estimate of the shape of the scattering pattern, with the magnitude being about 50% lower than the exact solution for $ka \leqslant 4$. A better comparison is shown in Fig. 11 for the magnitudes of the back- and forward-
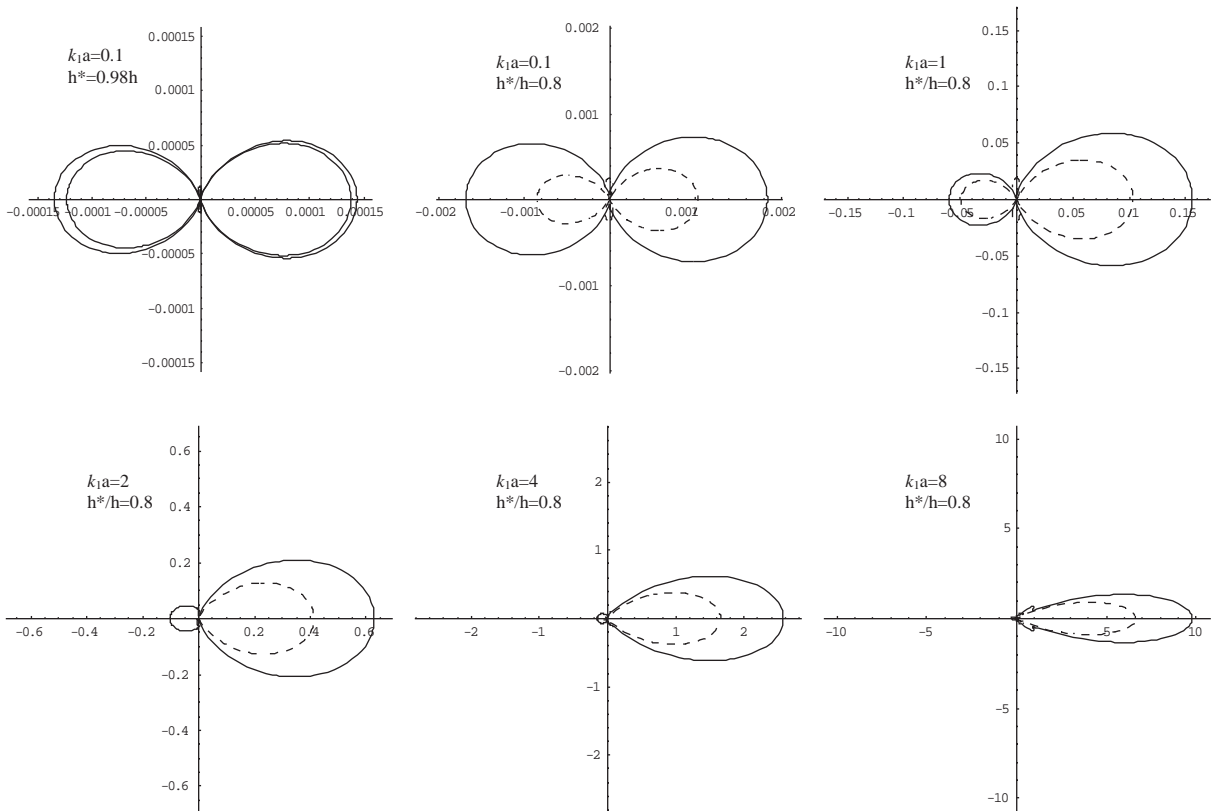
Fig. 9. Scattering patterns ($\left|S_2(\theta, k_1 a)\right|$) of flexural wave by a corrosion damage ($\omega = 0.1\omega_c$). Solid curves denote exact solutions while dashed curves denote Born approximation.

scattering amplitude. It can be seen that the Born approximation provides a good estimate of the forward-scattering amplitude for ka up to 6, but not for the back-scattering amplitude at large ka values.

5. Experimental validation

A square aluminum alloy plate (thickness = 1.02 mm, width and height = 508 mm) is instrumented with four piezoelectric transducers on one side, as illustrated in Fig. 12. The coordinates of the four transducers are given in Table 1. The electro-mechanical properties of the piezoelectric materials (APC850)[1], which are available from the manufacturer [34], are very similar to those of the Navy Type II (502) piezoelectric materials. The thickness and diameter of the piezoelectric transducer are 0.25 and 6.35 mm, respectively.

To investigate the wave scattering by an inhomogeneity, a circular mass made of bronze (diameter = 20 mm, height = 7.24 mm) was bonded to the plate. The location of the added-mass is

---

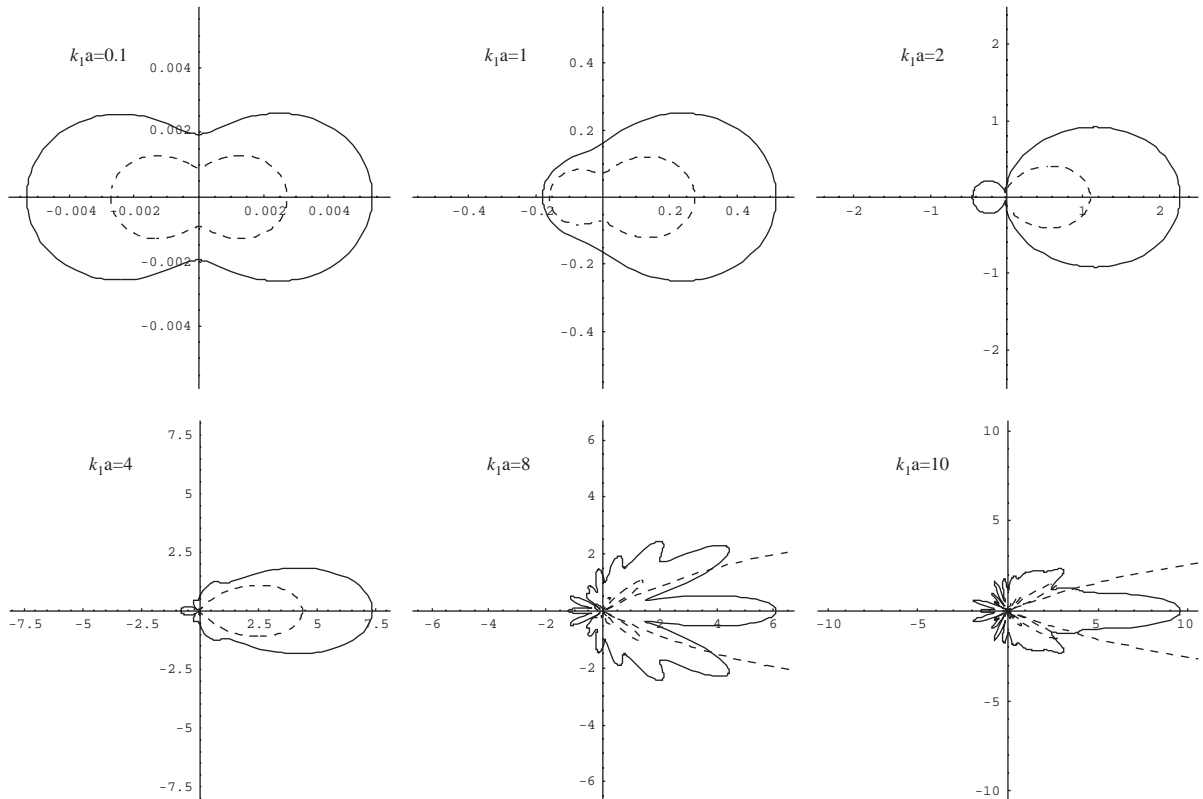[1]American Piezo Ceramics, Inc. (http://www.americanpiezo.com)

Fig. 10. Scattering patterns ($|S_2(\theta, k_1 a)|$) of flexural wave by a delamination damage ($\omega = 0.1\omega_c$). Solid curves denote exact solutions while dashed curves denote Born approximation solution.

also given in Table 1. The number 1 transducer was subjected to narrowband tone bursts, while the other three transducers were employed as sensors to measure the plate waves. A general representation of this experimental configuration is illustrated in Fig. 13. Prior to bonding the cylindrical mass to the plate specimen, experimental measurements were performed to determine the base-line response, denoted as $w^{(i)}$. Fig. 14 shows the sensor responses recorded at sensors 2, 3, and 4, when sensor 1 was actuated with tone burst excitation of peak voltage of 50 V. In the figure reflections by the plate boundary were filtered out, retaining only the first arrivals of the extensional wave (first pulse) and the flexural wave (second pulse). After a cylindrical mass was bonded to the plate, an experiment was carried out to determine the total wave field, denoted as $w^{(t)}$. Subtracting the base-line data from the total wave field yields the scattered wave $w^{(s)} = w^{(t)} - w^{(i)}$. The so determined experimental results are also shown in Fig. 14, together with the predictions by the present analytical method as outlined below.

For a circular piezoelectric sensor, its electric voltage response is proportional to the sum of surface strain $\in = \varepsilon_{xx} + \varepsilon_{yy}$. Denoting the transfer function of the sensor as $K_s(\omega)$, the Fourier transform of the sensor signal can be related to the Fourier transform of the surface mean strain
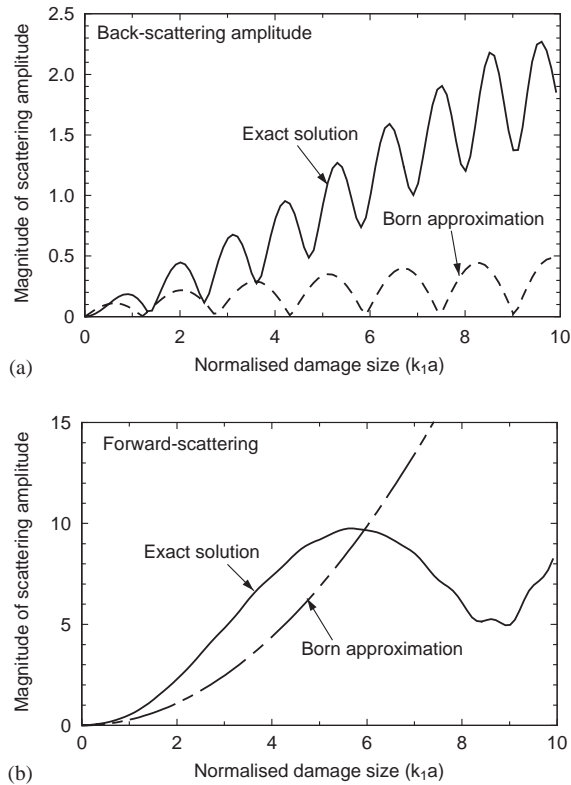
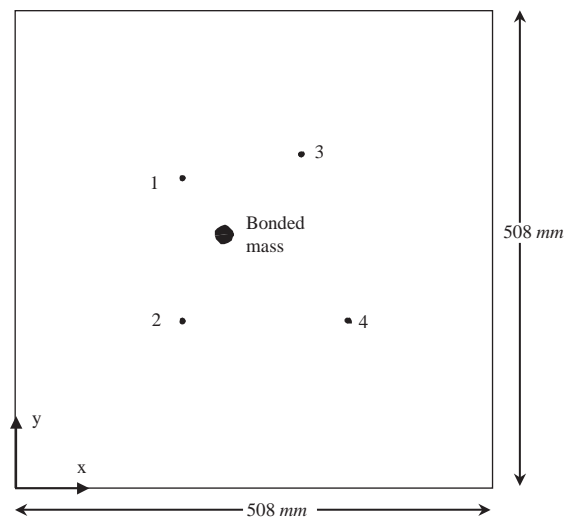Fig. 11. Magnitudes of (a) back- and (b) forward-scattering amplitudes for delamination damage ($D^* = D/4$).

Fig. 12. Specimen showing locations of sensors and bonded mass.

Table 1
Coordinates of transducers

Transducer or bonded mass	Coordinates (x,y) (mm)
1	(177.8, 330.2)
2	(177.8, 177.8)
3	(304.8, 355.6)
4	(355.6, 177.8)
Added mass	(222.3, 270.0)

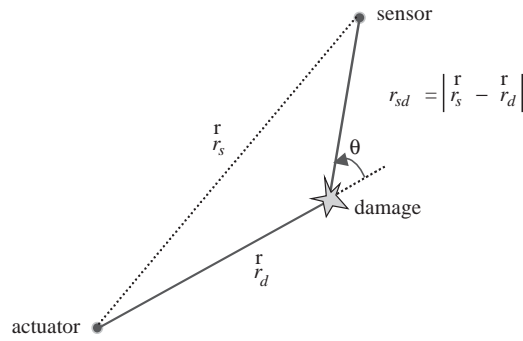Fig. 13. Configuration of an active sensor system for damage characterization.

$\hat{\in}(\omega)$,

$$\hat{V}_s(\omega) = \hat{\in}(\omega)K_s(\omega). \tag{33}$$

When a circular patch piezoelectric transducer is subjected to an electric excitation of $f(t)$, the surface mean strain at a distance r away is given by

$$\hat{\in}^{(i)}(\omega, r) = \hat{f}(\omega)g(\omega, k_1 r), \tag{34}$$

where $g(\omega, k_1 r)$ denotes the Green's function for a circular actuator [10]. Therefore, for the configuration shown in Fig. 13, the response of the sensor in the absence of damage or added mass can be written as

$$\hat{V}_s^{(i)}(\omega) = \hat{f}(\omega)g(\omega, k_1 r_s)K_s(\omega). \tag{35}$$

Similarly the sensor response to the scattered wave is given by

$$\hat{V}_s^{(s)}(\omega) = \hat{\in}(\omega, r_d)K_s(\omega)\sqrt{\frac{2}{\pi k_1 r_{ds}}}\, e^{i(k_1 r_{ds} - \pi/4)}S(\omega, k_1 r_{ds}). \tag{36}$$
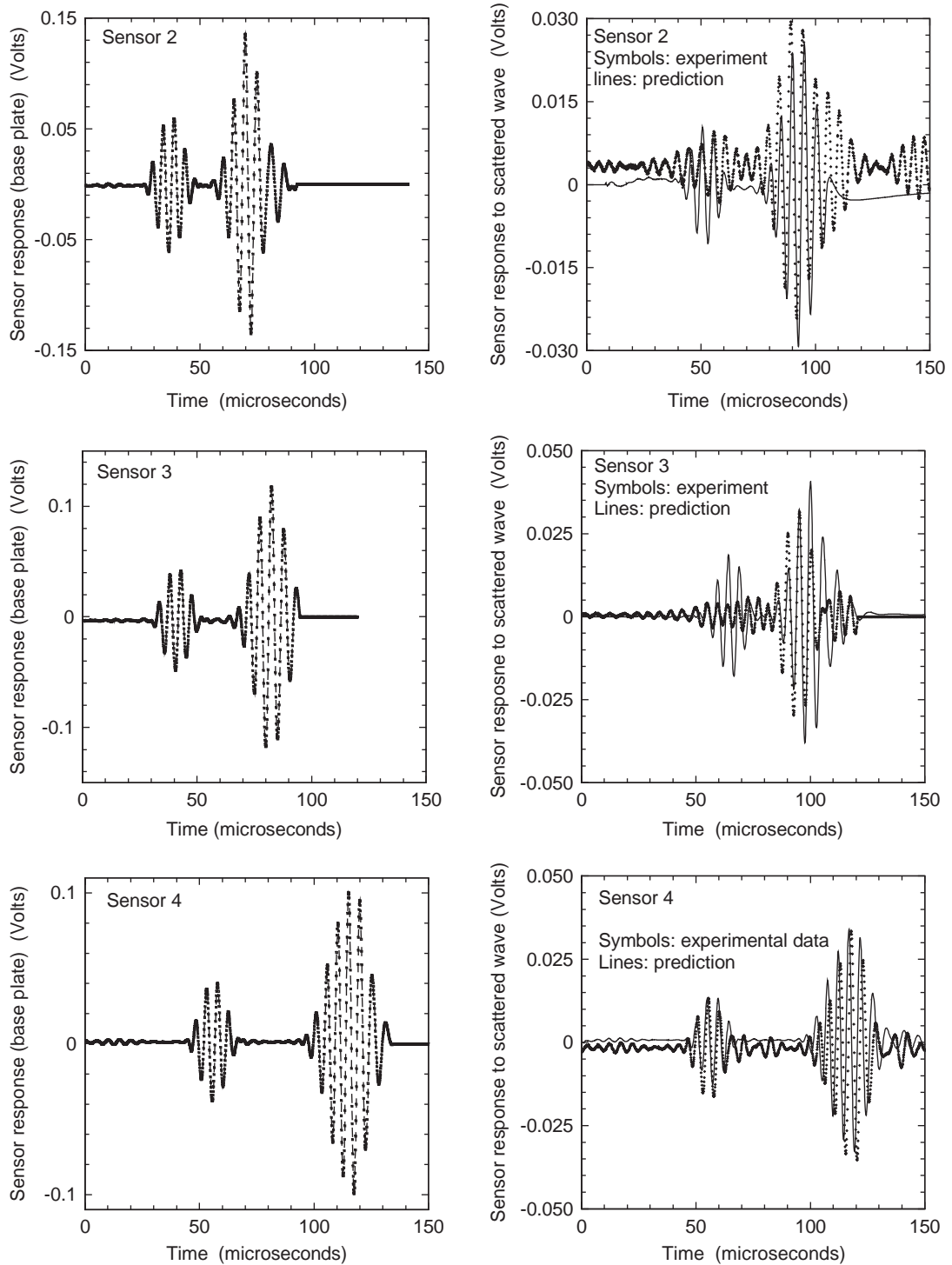
Fig. 14. Comparison of theoretical results with experimental data.

Combining Eqs. (35) and (36), the scattered signal can be related to the base-line signal,

$$\hat{V}_s^{(s)}(\omega) = \sqrt{\frac{r_s}{r_d}} \sqrt{\frac{2}{\pi k_1 r_{ds}}} \, e^{i[k_1(r_{ds}+r_d-r_s)-\pi/4]} \hat{V}_s^{(i)}(\omega) S(\omega, k_1 r_{ds}), \tag{37}$$

where S denotes the scattering amplitude, which is a complex number, determined by using the exact solution presented in Section 2.2. The predicted sensor responses to the scattered wave field are shown in Fig. 14, indicating a reasonable agreement. The discrepancies between the experimental data and theoretical predictions could be attributed to the coupling between the extensional wave and the flexural wave induced by the asymmetric nature of the bonded mass, which was not considered in the theoretical modeling.

6. Conclusions

To facilitate quantitative characterization of laminar damage using distributed network of piezoelectric sensors, analytical methods have been presented for a transversely isotropic plate containing a cylindrical inhomogeneity. Both exact solutions based on the wave function expansion method and an approximate solution based on the Born approximation have been developed for the scattered flexural plate waves. A good agreement has been observed between the theoretical prediction and the experimental results from a plate with a bonded cylindrical mass. The present results reveal that the scattering pattern is strongly dependent on the ratio of wavelength to the size of the inhomogeneity, which would help the selection of appropriate diagnostic frequency and the optimal placement of sensors. By comparing against exact solutions, the range of validity of the Born approximation has been determined for plate waves.

References

[1] N. Guo, P. Cawley, The interaction of Lamb waves with delaminations in composite laminates, *Journal of the Acoustical Society of America* 94 (1993) 2240–2246.
[2] D.A. Alleyne, P. Cawley, The interaction of Lamb waves with defects, *IEEE Transactions on Ultrasonics Ferroelectrics and Frequency Control* 39 (3) (1992) 381–397.
[3] N. Guo, P. Cawley, Lamb wave reflection for the quick nondestructive evaluation of large composite laminates, *Material Evaluations* 52 (1994) 404–411.
[4] A. Birt, Damage detection in carbon-fibre composites using ultrasonic Lamb waves, *Insight* 40 (1998) 335–339.
[5] J.L. Rose, Guided wave nuances for ultrasonic nondestructive evaluation, *IEEE Transactions on Ultrasonics, Ferroelectrics, and Frequency Control* 47 (3) (2000) 575–583.
[6] F.-K. Chang, Smart layer—built-in diagnostics for composite structures, in: *Smart Materials and Structures, Proceedings of Fourth European Conference on Smart Structures and Materials*, United Kingdom, 1998.
[7] S.H. Diaz Valdes, C. Soutis, Health monitoring of composites using Lamb waves generated by piezoelectric devices, *Plastics, Rubber and Composites* 29 (2000) 475–481.
[8] M. Lemistre, D. Balageas, Structural health monitoring system based on diffracted Lamb wave analysis by multiresolution processing, *Smart Materials and Structures* 10 (2001) 504–511.
[9] E.V. Malyarenko, M.K. Hinders, Fan beam and double crosshole Lamb wave tomography for mapping flaws in aging aircraft structures, *Journal of the Acoustical Society of America* 108 (2000) 1631–1639.

[10] L.R.F. Rose, C.H. Wang, Mindlin plate theory for damage detection I, *source solutions, Journal of the Acoustical Society of America* 116 (1) (2004) 154–171.

[11] J.F. Doyle, *Wave Propagation in Structures*, second edition, Springer, New York, 1997.

[12] C.H. Wang, L.R.F. Rose, Wave reflection and transmission in beams containing delamination and inhomogeneity, *Journal of Sound and Vibration* 264 (2003) 851–872.

[13] T. Grahn, Lamb wave scattering from a circular partly through-thickness hole in a plate, *Wave Motion* 37 (2003) 63–80.

[14] T.R. Kane, R.D. Mindlin, High-frequency extensional vibrations of plates, *Journal of Applied Mechanics* 78 (1956) 277–283.

[15] R.D. Mindlin, Influence of rotary inertia and shear on flexural motions of isotropic, elastic plates, *Journal of Applied Mechanics* 18 (1951) 31–38.

[16] J.C.P. McKeon, M.K. Hinders, Lamb wave scattering from a through hole, *Journal of Sound and Vibration* 224 (5) (1999) 843–862.

[17] Y.-H. Pao, Dyanamic stress concentration in an elastic plate, *Journal of Applied Mechanics* 29 (1962) 299–305.

[18] C. Vemula, A.N. Norris, Flexural wave propagation and scattering on thin plates using Mindlin theory, *Wave Motion* 26 (1997) 1–12.

[19] C. Vemula, A.N. Norris, Scattering of flexural waves on thin plates, *Journal of Sound and Vibration* 181 (1) (1995) 115–125.

[20] P. Fromme, M.B. Sayir, Measurement of the scattering of a Lamb wave by a through hole in a plate, *Journal of the Acoustical Society of America* 111 (3) (2002) 1165–1170.

[21] P. Fromme, M.B. Sayir, Detection of cracks at rivet holes using guided waves, *Ultrasonics* 40 (2002) 199–2003.

[22] G.E. Evans, *Antenna Measurement Techniques*, Artech House, Boston, 1990.

[23] L.R.F. Rose, C.H. Wang, Mindlin plate theory for damage detection II, scattering by flexural inhomogeneities, *Journal of the Acoustical Society America*, in press.

[24] C.H. Wang, L.R.F. Rose, Plate wave tomography for structural health monitoring, in: *Review of Progress in Quantitative Non-destructive Evaluation*, American Institute of Physics, 2002, pp. 1615–1622.

[25] T.D. Mast, I.N.A., R.C. Waag, Focusing and imaging using eigenfunctions of the scattered operator, *Journal of the Acoustical Society of America* 102 (2) (1997) 715–725.

[26] T.D. Mast, Wideband quantitative ultrasonic imaging by time–domain diffraction tomography, *Journal of the Acoustical Society of America* 106 (6) (1999) 3061–3071.

[27] T.D. Mast, Aberration correction for time–domain ultrasound diffraction tomography, *Journal of the Acoustical Society of America* 112 (1) (2002) 55–64.

[28] A.C. Kak, M. Slaney, *Principles of Computerized Tomographic Imaging*, IEEE Press, New York, 1987.

[29] A. Kotousov, C.H. Wang, Three-dimensional solutions for transversally Isotropic composite plates, *Composite Structures* 57 (2002) 445–452.

[30] A. Kotousov, C.H. Wang, A generalised plane-strain theory for transversely isotropic plates, *Acta Mechanica* 161 (2003) 53–64.

[31] Y.-H. Pao, C.C. Mow, *Diffraction of Elastic Waves and Dynamic Stress Concentration*, Crane-Russak, New York, 1973.

[32] Wolfram (2003), http://www.wolfram.com.

[33] F. Lin, A.I. Nachman, R.C. Waag, Quantitative imaging using a time–domain eigenfunction method, *Journal of the Acoustical Society of America* 108 (3) (2000) 899–912.

[34] APC, Physical and piezoelectric properties of APCI materials (850), American Piezo Ceramics Inc., Duck Run, Mackeyville, PA, USA, 2002. http://www.americanpiezo.com/materials/apc_properties.html.